



HAL
open science

R(refracted)-PIV measurements of water film flow: application to flow under a rolling tire

Arbia Ben Khodja, Serge Simoëns, Marc Michard, David Le Touzé, Corentin Hermange, Clément Poncet, Guillaume Oger

► **To cite this version:**

Arbia Ben Khodja, Serge Simoëns, Marc Michard, David Le Touzé, Corentin Hermange, et al.. R(refracted)-PIV measurements of water film flow: application to flow under a rolling tire. Journal of Visualization, 2022, 25 (6), pp.1151-1167. 10.1007/s12650-022-00848-5 . hal-03842859

HAL Id: hal-03842859

<https://hal.science/hal-03842859>

Submitted on 7 Nov 2022

HAL is a multi-disciplinary open access archive for the deposit and dissemination of scientific research documents, whether they are published or not. The documents may come from teaching and research institutions in France or abroad, or from public or private research centers.

L'archive ouverte pluridisciplinaire **HAL**, est destinée au dépôt et à la diffusion de documents scientifiques de niveau recherche, publiés ou non, émanant des établissements d'enseignement et de recherche français ou étrangers, des laboratoires publics ou privés.

R(Refracted)-PIV measurements of water film flow: Application to flow under a rolling tire

Arbia BEN KHODJA^{1,2,3}, Serge SIMOËNS², Marc MICHARD², David LE TOUZÉ³, Corentin HERMANGE¹, Clément PONCET¹ and Guillaume OGER³

¹La Manufacture Française des pneumatiques MICHELIN, Clermont-Ferrand, 63000, France.

²Univ Lyon, Ecole Centrale de Lyon, Univ Claude Bernard Lyon1, INSA Lyon, LMFA, UMR5509, Ecully, 69130, France.

³Ecole Centrale Nantes, LHEEA Research Department (ECN/CNRS UMR6598), Nantes, 44300, France.

Contributing authors: arbia.ben-khodja@michelin.com;
serge.simoens@ec-lyon.fr; marc.michard@ec-lyon.fr;
david.letouze@ec-nantes.fr; corentin.hermange@michelin.com;
clement.poncet@michelin.com; guillaume.oger@ec-nantes.fr;

Abstract

An analysis of the water flow generated by a tire rolling over a water film has been carried out on an experimental level. The present investigation is focused on a commercial tire with a winter V-shaped complex sculpture. Flow measurements were performed using an optical technique derived from the standard 2D-PIV, the so-called r(refracted)-PIV. Some specific image processing tools have been developed in order to take into account the jitter of the tire location inside the camera field of view when analyzing a set of independent runs. Considering the analysis of the flow either inside the grooves or in front of the tire, different approaches are proposed. On one hand, a geometrical segmentation of the grooves allows a flow analysis inside these tread elements. A characteristic water velocity deduced from measurements performed over a set of independent runs appears to correlate with the position of the segment under consideration along the contact patch area (CPA). It has been considered as the hydrodynamic signature of the present tread design. On the other hand,

inside the water-bank in front of the tire, an ensemble averaging process of the local velocity is performed to show the influence of groove presence at small scale and the impact of tread design at large scale.

Keywords: Hydroplaning, flow visualization, Particle Image Velocimetry, complex geometry, tire tread

1 Introduction

The hydroplaning is a situation well-known by car drivers that may lead to fatal accidents. It is a gradual phenomenon directly linked to the vehicle velocity where the tire loses its contact with the ground under rainy conditions [1]. Because of the high speed, the tread grooves are not able to drain water quickly enough anymore, leading to an increasing pressure of the fluid in contact with the tire. The fluid lift is therefore increased as well, deforming the tire, and reducing its contact area with the ground [2][3]. Numerical studies have been made in the purpose of better understanding this complex problem and seeking in the end an optimization of the tread design [4] [5] [6] [7]. Combined experimental and numerical works have also been conducted focusing on the comparison of global parameters like the skid resistance and the hydroplaning speed [8] or also the evolution of footprint shapes with the velocity [9]. In the late 60s, testing facilities for the hydroplaning investigation helped showing the importance of the tread pattern by comparing breaking force coefficient of smooth tires with treaded ones [10]. More recently, experimental investigations have been performed involving different water heights, tread depths and inflation pressures leading to the comprehension of the main factors leading to the loss of the contact surface [11]. However, the first local quantitative velocity investigation during situations that could lead to hydroplaning has been experimentally proposed by Cabut et al. [12] based on an extended Particle Image Velocimetry (PIV) technique, the so-called r(refracted)-PIV. This dedicated measurement method opens the possibility of a deeper investigation of the water flow inside the grooves located in the CPA and also in the region around the CPA during the rolling of a tire over a water film. For this aim and to analyse their first results obtained with such a method, Cabut [13] and Cabut et al. [14], [15] defined some first parameters to describe quantitatively flows inside grooves and outside the CPA. In [14] they focused on the water-bank (region in front of the tire) and shoulder zones whereas in [15] they focused their interest on flows inside the longitudinal grooves of a summer tire (Michelin Primacy 4). Furthermore, for a given transverse groove, Cabut [13] developed a velocity averaged (inside the groove domain) parameter and plot it as a function of the longitudinal location of this transverse groove (barycenter of the integration domain). Such result, never published, show how water ejection from the CPA, is dependant on the location of the groove inside the CPA during the rolling process. This major result is carried

on in the current study for a different type of tire tread. In so, the exact same experimental set up as in Cabut and partners' work, but with a different tire with a different zone complexity is used here to lead this groove analysis. In the present work, the local velocity inside the grooves is calculated through a segmentation process adapted to the complexity of the studied tread design. A commercial winter tire with transversal grooves and a central zigzag part is considered. At the best of our knowledge, the splitting of the groove geometry, for local average, is an analysis that has never been published before and even more never applied to flow analysis of transversal grooves. To conclude, this work is the continuity of Cabut's work with the permanent research of a specific universal behavior whatever the tread design. Such approach is necessary for a quantitative description of the flow circulation inside a specific tire tread and will eventually help us improve our knowledge of the complex mechanism that lead to the hydroplaning situation.

The layout of the present paper is as follows. In section 2 we present the experimental setup, with a focus on a specific r-PIV arrangement using refraction at a solid/liquid interface. Some specific tools for data and image processing are described in order to consider the random position of the tire when performing a set of independent measurements. Some specific features of the flow inside directional grooves, as well as in the water-bank located in front of the contact patch area are given and discussed in section 3. Finally, some conclusions and perspectives are drawn in section 4.

1.1 Abbreviations and notations

- A6: MICHELIN Alpin 6 205/55 R17 commercial tire
- CPA: Contact patch area
- H_w : Depth of the water film (in *mm*)
- L_x : Length of the contact patch area in X-axis direction (in *mm*)
- N : Number of runs given one set of operating parameters (V_0, H_w)
- V_0 : Car speed (in $m.s^{-1}$)
- $V^* = V/V_0$: Dimensionless velocity
- WB: Water-bank
- $x^* = x/L_x$: Dimensionless abscissa

1.2 About the tread design

In this work we focus on a commercial winter tire currently designated as A6. We consider a worn state of the tire leading to a remaining tread depth of 2mm, while for a new tire it is about 8mm. We give in Fig.1 a depiction of the A6 tread in both new and worn states with some dimensions to give the reader an order of magnitude concerning the tread design. The central groove has a zigzag shape connected to directional grooves extending from the center to the shoulder of the tire and segmented into three nearly straight segments. Note that for acoustic issues the actual width and spacing of directional grooves is not strictly equal for all of them, and dimensions given on the left in Fig.1 are

averaged typical values. Moreover, some segments of the directional grooves have a worn indicator producing periodically a local geometric restriction of the flow in the groove as the car is rolling. Nevertheless, these indicators do not appear to influence the flow inside the central groove and are rarely located in the directional grooves in our database. In comparison, such indicators are of first order importance inside longitudinal grooves for summer tires as the one investigated by Cabut et al.[15]. The third kind of grooves of interest are the ones between two adjacent directional grooves, herein after simply identified as “connecting grooves”. Finally, the tire has what is known as an “evolving” tread, which results in the progressive appearance of sipes during the wear process among other modifications. Nevertheless, the spatial resolution of PIV measurements is not sufficient for capturing the flow inside these sipes because of their reduced width. Therefore, in this work we only focus on the flow in the central, directional and connecting grooves.

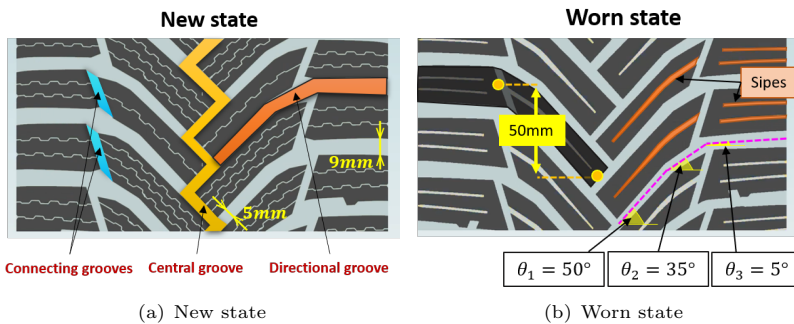


Fig. 1: Details of the A6 tread design in a new (left) and worn (right) state

2 Refracted-Particle Image Velocimetry (r-PIV) measurements

The PIV technique has been previously used for the measurement of the air flow around the tire in the aim of aerodynamic drag study [16][17]. However, to the best of our knowledge, the PIV has been used for the first time in a hydroplaning application including a liquid phase by Cabut et al. [12]. The authors derived a specific method from the classical planar PIV, the so-called r-PIV (refracted-PIV), for application to a tire of a real car rolling through a puddle of water. In this section we introduce the experimental facility used in this work, then we present some specific processing tools of PIV images for such a complex tread pattern.

2 REFRACTED-PARTICLE IMAGE VELOCIMETRY (R-PIV) MEASUREMENTS

2.1 Experimental set-up

Measurements are performed on an in-situ track at Michelin Technology Center of Ladoux (Cébazat, France). The dedicated area is a dry straight road with a transparent portion made of a thick PMMA block that is embedded to the ground and was used for previous studies [11] [14]. The studied tire will roll on this transparent window, on which a water film is initially at rest, delimited by a seal and height controlled. For safety issues all emitting and receiving optics are located under the ground level in a dedicated room. Therefore, it is not possible to generate a planar light sheet parallel to the ground as should be done with a standard 2D PIV measurement system and a specific optical arrangement is needed for the targeted application. The overall scheme of the installation is presented in Fig.2(a).

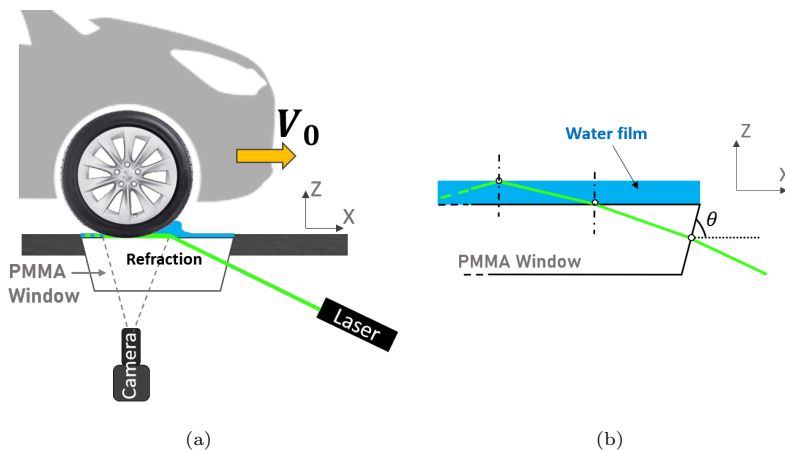


Fig. 2: Scheme of the in-situ r-PIV installation (a) and detail of the refraction processes of the laser sheet at the air/PMMA and PMMA/water interfaces (b)

2.1.1 Emitting optics characteristics

The experimental setup has previously been detailed by Cabut et al. [14], [15]. Let us only recall that the source light is a dual cavity pulsed laser emitting at a wavelength of 532nm. The light sheet generated at the exit of the emitting device is directed towards the inclined face of the transparent window depicted in Fig.2(b). The angle θ is equal to the theoretical angle predicted by Snell-Descartes laws for full refraction at the PMMA/water interface for an incoming light sheet normal to the inclined face. A small angle of the light sheet with the normal allows, after refraction, the propagation of the light sheet inside the liquid film, with a high spreading rate. Therefore, for a small thickness of the water film, the vertical intensity profile $I(z)$ of illumination is nearly uniform in the area of interest, and the liquid film is illuminated in the volume, introducing

6 2.1 Experimental set-up

some bias in velocity measurements for inhomogeneous actual velocity profiles in the vertical direction. Such bias due to both emitting and receiving optics have been analyzed by Cabut et al. [12].

2.1.2 R-PIV seeding

The tracers used in this application are fluorescent particles doped with Rhodamine B allowing a high signal-to-noise ratio, as soon as a narrow-band filter centered around $584nm$ with a bandwidth of $\pm 10nm$ is mounted on the camera lens. The particles are rather spherical with a nearly Gaussian diameter distribution with a mean value of $d_p = 35\mu m$ and a standard deviation of about $5\mu m$. To quantify inertia effects of particles, we have evaluated their Stokes number $St = \frac{\tau_p}{\tau_f}$ where τ_p is the particle response time and $\tau_f = \frac{L_0}{U_0}$ the characteristic time scale of the flow. Inside the CPA (contact patch area: region where the tire is in contact with the ground), L_0 can be taken as the CPA length L_x and U_0 as the streamwise velocity V_x inside the grooves. The relaxation time is calculated as $\tau_p = \frac{\rho_p d_p^2}{18\mu}$ where $\rho_p = 1.19kg/m^3$ is the particles density and $\mu \approx 1.10^{-3}Pa.s$ (20 °C) the water dynamic viscosity. We can find that $St < 10^{-5}$ which is small enough and we can then consider that the particles perfectly follow the fluid.

2.1.3 Receiving optics characteristics

Pairs of images are recorded with a double frame sCMOS camera with a resolution of 2560×2160 pixels in the streamwise and spanwise directions respectively. The dimensions of the field of view are $224mm \times 190mm$, and the calibration factor is 0.09 mm per pixel. The focal distance is equal to $100mm$, the working distance between camera lens and the water film has been fixed to nearly $1150mm$ and the lens aperture fixed to $5:6$.

2.1.4 Synchronization of the acquisition

To ensure the synchronization of the laser and the camera with the rolling of the tire on the window, a programmable timing unit (PTU) is used in combination with the commercial software DaVis 8. Optical sensors located some meters before the water puddle calculate the actual car's speed V_0 and generate a trigger signal with a time delay. This delay is computed with a real-time processor and adjusted in order to trigger the PIV system when the tire is at a pre-defined location inside the camera's field of view, whatever the value of V_0 . The time-delay δt between the two-pulses of the laser is adjusted to the vehicle speed, e.g., $\delta t = 225\mu s$ for $V_0 = 11.11m.s^{-1}$. Before each run, the driver sets the car in position in the beginning of the track and waits for the water film to reach its targeted value H_w . When the test starts, a process of rolling, illuminating, and image recording is achieved. For the analysis of the flow repeatability, since PIV measurements are not time-resolved with the system, the overall procedure is repeated over a set of N independent runs for a fixed couple of operating parameters V_0 and H_w .

2 REFRACTED-PARTICLE IMAGE VELOCIMETRY (R-PIV) MEASUREMENTS

2.1.5 Water depth

The water film depth is regulated by an ultrasound probe located on the track. The standard deviation of H_w over the set of N runs is around 3% for low wind conditions. We choose $H_w = 1.5\text{mm}$ in the present r-PIV experiments; this height is a good compromise between European regulations for breaking tests on wet roads and the homogeneity of the water depth on the window. We note that a higher water depth is more penalizing from the hydroplaning perspective.

2.2 Image acquisition and processing

The velocity field is generated using the commercial software DaVis. The cross-correlation between a pair of images is performed with an iterative process using interrogation areas of decreasing size. The initial size 96x96 pixels is dictated by the maximum displacement of seeding particles. The final size 32x32 pixels with an overlapping factor of 75% results of a compromise between signal-to-noise ratio and spatial resolution. The minimum interrogation window size is therefore comparable to half the width of the central groove, and the mesh grid obtained for the selected overlapping factor is 0.7mm . Note that due to the presence of geometric masks as windows are shifted (for overlapping) to the border of a groove, the spatial resolution is locally improved. For some regions of the images, tests were done to ensure that a smaller window size, down to 16x16 pixels, does not change or improve the results obtained with the present parameters.

Before generating the velocity field of each run, a geometric virtual mask is applied on the raw images. The mask generation is one possible source of variability in the results presented in section 3. It is a sensible task since from one image to another not only the tire deformation is not the same due to the dynamics of the fluid, but also the image illumination changes. The purpose of the mask is primary to remove regions without seeding particles (out of fluid flow regions), but also to enhance the cross-correlation quality near the groove's borders. The mask is generated using our own image processing algorithm based on binarization, Gaussian blurring as well as other morphological operations, e.g., closing and dilation. We give in Fig.3(a) an example of a raw image, the corresponding image with its geometric mask in Fig.3(b) and the velocity field obtained by cross-correlating a pair of masked images recorded for a given run in Fig.3(c).

This mask determination method is different from Cabut's work in which a manual process is adopted [13]. The present procedure should remove the uncertainty introduced by the operator factor. In addition, despite the driver's skills, the location of CPA inside the field of view can undergo some disparity from one run to the other. We show in Fig. 4 raw images for four different runs to highlight the difference of positioning of the tire on the window. The

8 2.3 Generation of (X,Y)-offsets for CPA collapse

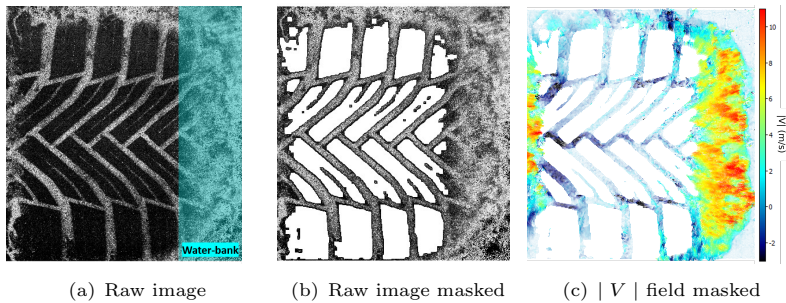


Fig. 3: Raw intensity image of run 1 from r-PIV acquisition with a highlight of the water-bank region (a), then the same image on which we apply a binary image called a mask (b) and the velocity field associated generated from the cross-correlation processing (c) of the A6 tire in a worn state at $V_0 = 11.11 m.s^{-1}$ and $H_w = 1.5 mm$

variability appears to be mainly in the spanwise direction Y; a small jitter in the X location of the CPA can be explained by small departures of the actual water film depth from the targeted one. At this stage the origin O is the one resulting from the calibration of the camera, and its location inside the field of view is arbitrary.

2.3 Generation of (X,Y)-offsets for CPA collapse

We intend to analyze the flow in the water-bank (highlighted in blue in Fig.3(a)) and inside the grooves for a set of independent runs. Therefore, the location of the CPA, or at least its leading edge, needs to be collapsed to define a common coordinate system for all the velocity fields, with a common origin O with some physical relevance with the flow structure around the tire and inside the CPA. For a reference run, the image Img_0 is first chosen, then the (X,Y) offsets of the other images (runs), relatively to Img_0 , need to be computed against Img_0 .

Two different strategies are proposed to generate the X-offset:

- **Intensities (or grey level)-based strategy:** The main idea is to use the grey-level intensity distribution inside raw images. This method has previously been used by Cabut et al [15] for a tire model with four central longitudinal grooves. In that case, the X-offset for different runs was deduced from the grey-level profile along a narrow band including the central rib with straight edges; such profile is nearly uniform with a very low noise level for the region located inside the CPA and presents a strong gradient near the front edge of the CPA due to the contribution of seeding particles present in the liquid phase, just in front of the central rib.
- **Velocity-based strategy:** This method is based on a quite different idea. The different tires present the common property to push the liquid to the front, with the appearance of the so-called water-bank with a peak value on the V_x velocity profile, bounded by relatively sharp falling and raising edges.

2 REFRACTED-PARTICLE IMAGE VELOCIMETRY (R-PIV) MEASUREMENTS

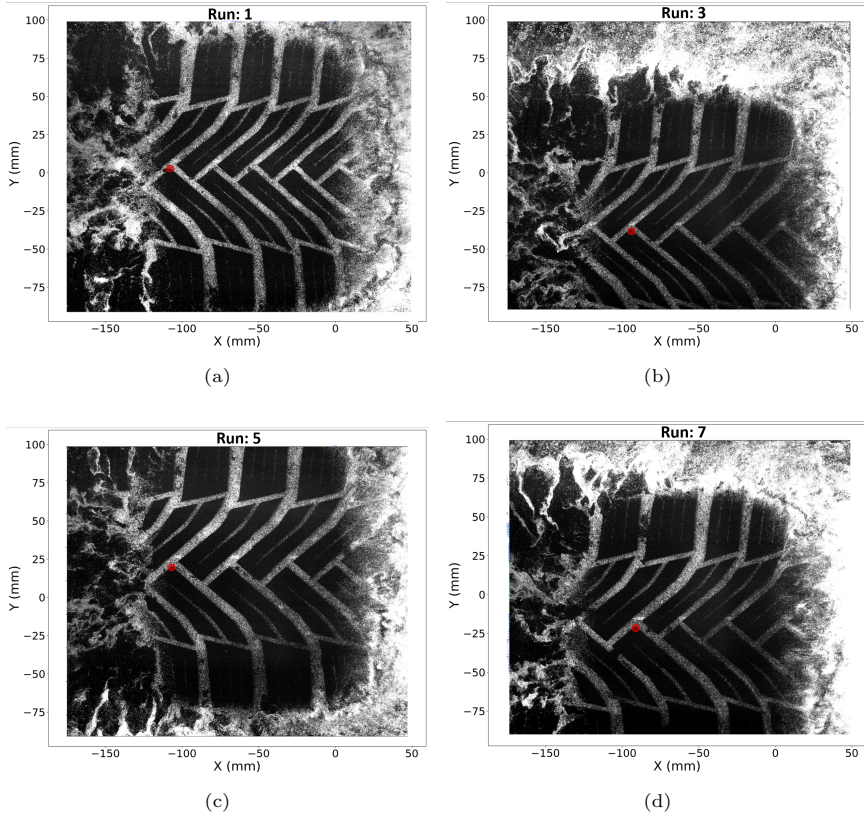


Fig. 4: Raw intensity images (Frame 0) for four independent runs. The red dot on images shows the relative position of a given arbitrary point located on the edge of the central zigzag groove.

Most of the existing tire models also generate locally a plateau in the V_x profile behind the tire, with a zone of sharp gradient near the CPA trailing edge, as depicted in Fig.5. The X-offset is then deduced from the displacement corresponding to the peak value of the cross-correlation between V_x velocity profiles. The main assumption for this method is that the global shape of the velocity profile remains nearly similar from one run to the other. Therefore, variations due to potential turbulence or two-phase flow influences are hypothesized negligible compared to velocity field determination error levels.

For the tire considered in this study, its complex groove shapes (zigzag and directional grooves) leads to much noisier grey-level profiles inside raw images in the X-direction near the tire mid-plane, than for a tire with longitudinal grooves. Therefore, the peak-detection of the cross-correlation between

grey-level profiles is somewhat difficult to obtain. Hence the choice to apply the second strategy based on the analysis of velocity profiles.

The first step is to determine the Y-offsets over the N runs. An easily identifiable point on each image is selected using the tread pattern of the tire, e.g. the top of the central zigzag groove depicted with red dots in Fig. 4. The Y-offsets are calculated via the rule:

$$\text{Y-offset}_j = \text{Ycoordinate}_{\text{Img}_0} - \text{Ycoordinate}_j \text{ for } 0 \leq j \leq N - 1$$

At this point, we are able to collapse at the best the N images along the Y-axis. The X-offsets are then determined as follows. We note V_{jI} the Y-shifted velocity field of the run j that is computed for masked images according to Sec. 2.2. In order to remove some potential small-scale noise, the velocity field is then spatially averaged along Y in a band centered around $y = 0$, as shown in green in *Img*₀ (Fig.5(a)). The resulting spatially Y-averaged velocity $V_{jII}(x)$ is related to $V_{jI}(x, y)$ by the relation:

$$V_{jII}(x) = \frac{1}{y_2 - y_1} \sum_{y_i=y_1}^{y_2} V_{jI}(x, y_i) \quad (1)$$

Then comes the actual correlation step between the $V_{jII}(x)$ profiles and the $V_{0II}(x)$ one. The curves of $V_{jII}(x)$ are plotted together on Fig.5(c), this for each j ($0 \leq j \leq N - 1$). X-offset _{j} are determined corresponding to the maximum of correlation for each case. Each offset corresponds to the translation for the best curve shape matching. Therefore, this method tends to overlay the images according to the position of their water-bank. In case of the A6, the Fig.5(d) indicates the final shifting; even if the peak value of the profiles undergoes some variations from one run to the other, the collapse of the positions of the rising and falling edges of velocity profiles is very satisfactory.

At this stage, the location $x = 0$ is common for all runs but remains somewhat arbitrary. In Fig.5(b) the CPA region is bounded by the dashed vertical lines in the intensity profile along X-axis, it corresponds to the area where the illumination is the lowest since the tire is in contact with the ground. We decide to define $x = 0$ as the location of the right dashed line where the grey-level gradient increases suddenly. Concerning the position of $y = 0$ it has been chosen so that it corresponds to the center of the middle zigzag groove. With this choice, we introduce a natural separation between the flow inside the grooves of the CPA ($x < 0$), and in the water-bank in front of the tire ($x > 0$) which is the region where the water velocity and the pressure are the highest. This last region is responsible for the main part of the fluid lift and therefore of the reduction of the CPA when the car velocity increases. In the rest of this document, V_x^* denotes V_{II}/V_0 .

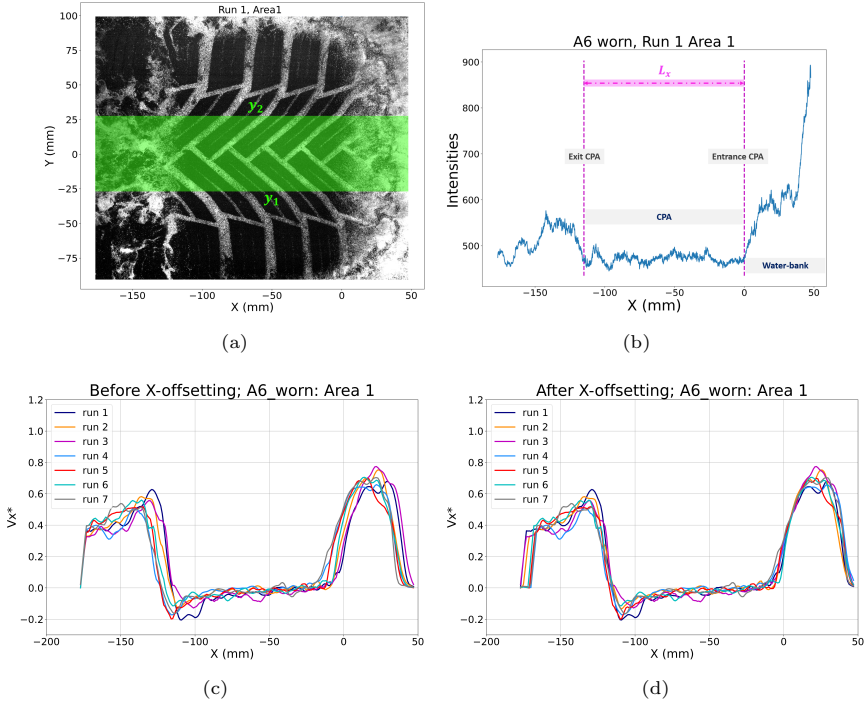


Fig. 5: Area 1 highlighted in green on raw image of the A6 at $V_0=11.11m.s^{-1}$ and $H_w = 1.5mm$ (a), image intensities space averaged along Y-axis in Area 1 (b) and V_{x^*} space averaged along Y-axis in Area 1 before (c) and after (d) X-offsetting

3 Results

We present in this section results obtained for the A6 tire in a worn state at $V_0 = 11.11m.s^{-1}$ ($40km/h$) and $H_w = 1.5mm$. Our objective in this part is to see in what extent parameters and normalized quantities could be used for studying another tread design tire, and in what extent they could help understanding flow circulation inside and outside the CPA zone.

3.1 Single run

We give in Fig.6 the velocity magnitude $|V|$ for one run of the A6 tire. In this section we will study the water flow in different zones of the CPA in order to estimate the preferential directions of the water inside the grooves and the evolution of the velocity inside a directional groove depending on its position in the CPA. The objective being first to have an idea about the flow structure along the different grooves and how water is moving from the head of the CPA to the rear or to the shoulders.

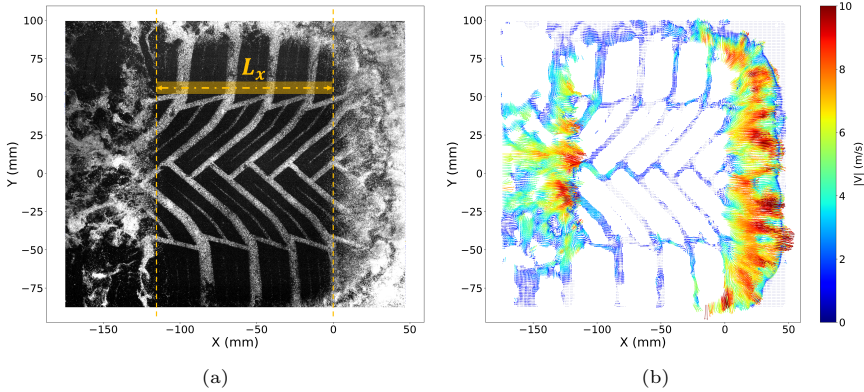


Fig. 6: Raw r-PIV image (a) and its associated velocity field $|V|$ (b) (run 1)

3.1.1 Flow inside the central zigzag groove

We start to analyze the velocity inside the central groove. We show in Fig.7 the field of velocity magnitude inside this groove from the previous shown global velocity field (Fig.6(b)). The intensities are deduced from the colormap. We focus here on the area between $x = -115\text{mm}$ and $x = 0$ which corresponds to L_x , the length of the CPA (highlighted in Fig.6(a)). We normalize the X-axis by L_x and we note $x^* = X/L_x$ the dimensionless abscissa. Note that this length is chosen following the first work done by Cabut et al. [15] demonstrating its use for self-similarity trends for velocity profiles along straight groove. This is the first attempt to use the same kind of analysis for a tire that has a complex central groove. Identically, the velocity is normalized by V_0 as in Cabut's work. First, we can see that we have a rather good resolution and the flow is well captured despite the complex geometry of the tire tread. Second, we observe that the flow is evacuated mainly from the front of the CPA ($x^* = 0\%$) to its rear ($x^* = -100\%$), and it is accelerating near the end. We give in Fig.8 the values of $V_x^* = V_x/V_0$ and $V_y^* = V_y/V_0$ space Y-averaged in the central groove ($-7\text{mm} \leq y \leq 7\text{mm}$) and plotted along the X direction. The Y-averaging is used to show the velocity trends inside the groove. As stated, the flow is accelerated till the rear of the CPA and V_x^* reaches around -0.3 near $x^* = -85\%$ while V_y^* reaches 0.2 in the same position. However, the peak values of V_y^* decrease from the rear to the beginning of the CPA. This can be due to the deformation of the tire when it leaves the CPA, the tread portions are suddenly relaxed and widen the central groove, accelerating the water flow to the end of the CPA. Furthermore, we can see in Fig.8(b) how the flow is disturbed due to the connections between this central groove and the directional grooves (highlighted with arrows) especially near $x^* = -90\%$ and $x^* = -70\%$. This disturbance is well captured in the upper half of the central groove while it seems weaker in the lower part.

This gives us some first quantitative and absolute information on the groove

flow. It is clear that more quantitative analysis has to be conducted and more particularly a referential linked to the variable axis along the groove and its corresponding perpendicular counterpart has to be defined. Note that for this present work we will do such analysis in section 3.1.4. Nevertheless, we will now present some description for another zone in order to have a final coarse description of the flow in the whole CPA region.

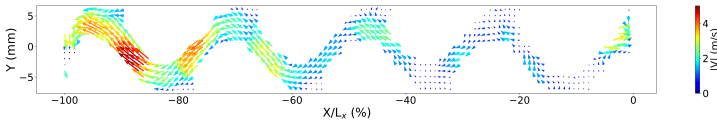


Fig. 7: Visualization of $|V|$ field inside the central groove (run 1)

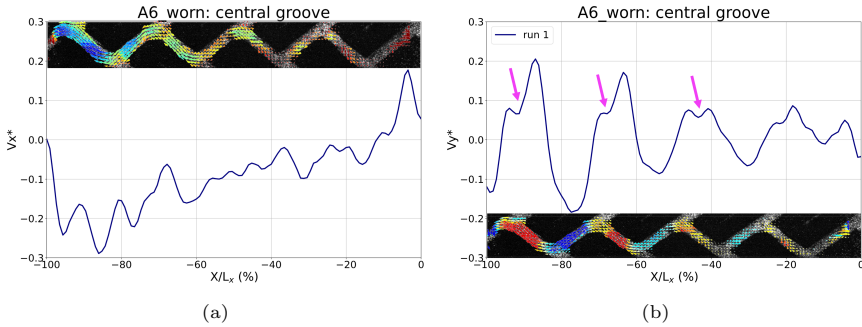


Fig. 8: V_x^* (a), V_y^* (b) profiles spatially averaged along Y-axis in the central groove (run 1). Colors on the colormaps correspond to the magnitude of the corresponding velocity component

3.1.2 In the directional grooves

We are interested here in analyzing the velocity field V_y in the directional grooves (those leading from the previously studied center groove to the tire shoulders) in order to show how water could be evacuated from the central zone. We call this region Area 2 (highlighted in green in Fig.9(b)). We can see in Fig.9(a) that along the CPA, y-averaged V_y^* goes from -0.2 for $x^* \approx -95\%$ to nearly zero between $x^* = -60\%$ and $x^* = -10\%$. Note here that as the Y-averaging is done over all Area 2 width, V_y^* is determined whatever the x^* location. Such results couldn't be compared to Cabut's results in the same region as in the present case contribution of velocity field comes exclusively from the transverse grooves. For this reason, such analysis is difficult to consider for a comparison with other tire treads in order to determine the drainage process. This actually requires the use of a parameter accounting for averaging

14 3.1 Single run

in the axial groove direction (or perpendicularly). This is what will be defined in part 3.1.4.

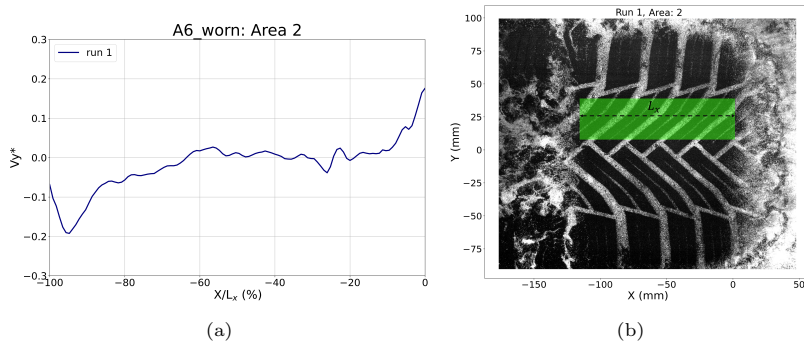


Fig. 9: Evolution of V_y^* (velocity y-averaged in the region Area 2) (a) and highlight of this region on raw image of run 1 (b)

In describing the instantaneous run, we show in Fig.10 an enlargement of the directional grooves, one close to the end of the CPA (pink dashed) and another close to the water-bank (orange dashed). We can clearly see how the water flow is directed to the central groove in the first case and how it is nearly stopped in the second one. This can partly explain the acceleration of the flow in the central groove that we have observed close to the end of the CPA (Fig.7 and Fig.8). The directional grooves supply the central one in this region of the CPA. Close to the water-bank it is rather the opposite, and the water flow goes from the central groove to the directional groove, but the velocity is rather low (less than $1m.s^{-1}$). Such coarse analysis shows the necessity to define a local referential for the grooves. At the best of our knowledge, this will be done for the first time in the part 3.1.4 for all present grooves of the same tire, separating the central zone from the border ejection zone.

3.1.3 Near the shoulders

To focus on the flow close to the shoulders, we define as previously a longitudinal band delimited transversally that we call Area 3 (Fig.11(b)). In Fig.11(a) we note that the zero velocity corresponds to the zone outside the grooves. The water is channeled inside the central groove ($V_y^* < 0$) in the rear of the CPA at a maximum velocity around $-2m.s^{-1}$. But for $x^* \geq -70\%$, it is directed from the CPA to the outside ($V_y^* > 0$). This flow dynamics have also been observed in the case of the Primacy 4 tire in a new state in the work of Cabut et al. [15] considering the analysis of C-type transverse grooves. The authors showed a correlation between the location of the groove along the X-axis and the velocity inside the groove : water is ejected outside for a groove located at the beginning of the CPA and sucked inside at the end of the CPA. This

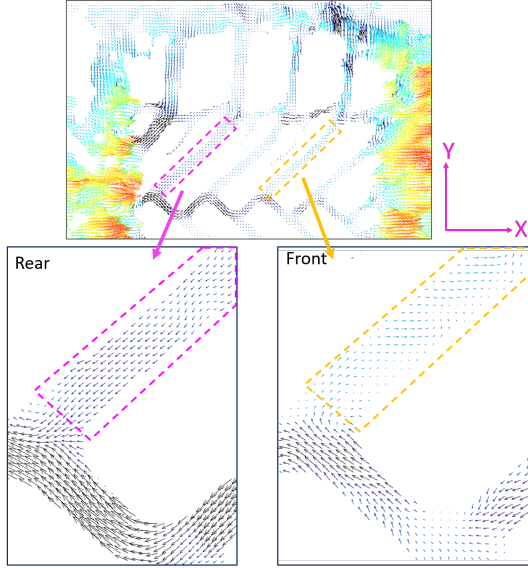


Fig. 10: Enlargement of the directional grooves at the rear (left) and at beginning (right) of the CPA

behavior was suggested to be related to the compression and relaxation of the rubber in the inlet and the outlet of the CPA. In our case, the correlation observed between the velocity inside the Area 3 and the position X/L_x is studied in more detail in section 3.1.4 for several repetitions and thus different positions of the directional grooves in the CPA.

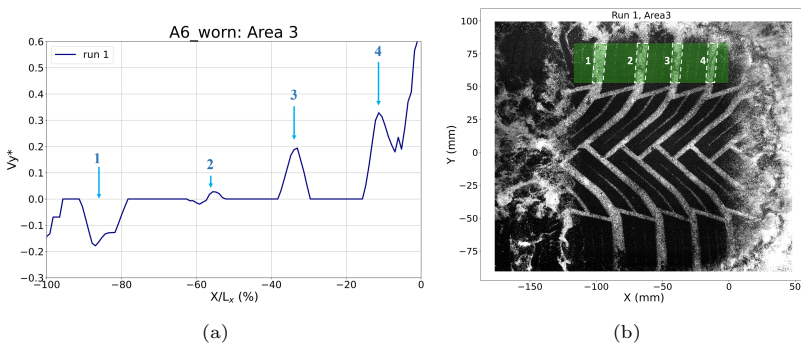


Fig. 11: Evolution of V_y^* that is obtained from the velocity Y-averaged in the region Area 3 (a) and highlight of region Area 3 on raw image (b) (run 1)

Finally, the directional groove at $x^* = -55\%$ of L_x (number 2 in Fig.11) does not really play a role of drainage here considering the very low velocity

inside it (around $0.5m.s^{-1}$). We give in Fig.12 an enlargement of the two rear directional grooves where we can see the difference of the flow dynamics from one groove to the other. We can note a difference in the grooves' width. This can be explained by the difference that exists in the tread pattern to reduce tire noise.

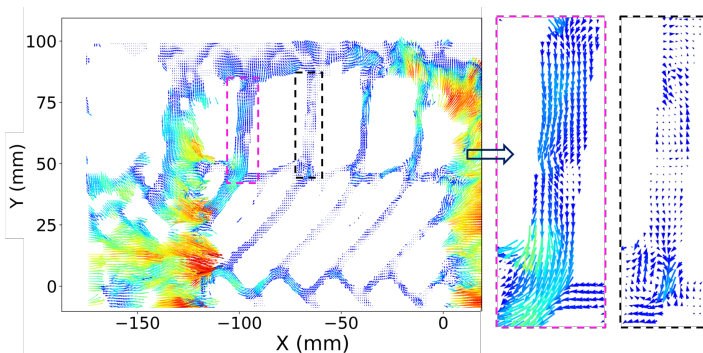


Fig. 12: Enlargement of the two transversal grooves at the end of the CPA (number 1 and 2 in Fig.11)

3.1.4 Definition of a local referential inside grooves

We now will generalize the local average parameter defined by Cabut [13] simultaneously for all transverse grooves involved in the drainage process from the CPA zone to outside. One of the main issues is to determine if the flow is sucked inside a groove or pushed outside it, depending on its x -position along the CPA. For that purpose, in a first step we define a new local referential (\vec{u}, \vec{v}) that follows the directional groove direction. We split each groove inside the CPA into three straight segments following roughly their change in direction from the shoulder to the central part of the CPA. We give in Fig.13(a) an example of the segments' definition for one of the directional grooves where \vec{u}_k ($k = 1, 2, 3$) is the vector defining the orientation of segment k . From now on we call simply \vec{u} the unit direction vector of the groove, and we focus on the velocity component $V_u = \vec{V} \cdot \vec{u}$. As shown in Fig.13(a), we have five directional grooves for each run. We call Groove 1 the directional groove near the end of the CPA till Groove 5 the directional groove near the water-bank following the X-axis orientation. A similar segmentation of the zigzag central groove is performed using nine elementary straight segments (Fig.13(b)). In a second step, we define inside each segment a characteristic fluid velocity $V_{u_{mean}}$ as the value of V_u spatially averaged along its width and length. If we have in mind that every velocity vector measured with the r-PIV technique is in fact the result of seeding particles which are randomly located and illuminated at different Z altitudes, we can consider that $V_{u_{mean}}$ is a global indicator of the velocity inside the volume corresponding to a segment. Finally, in a third step

we define the location x of a segment as the x -value of the geometric barycenter of the segment under consideration.

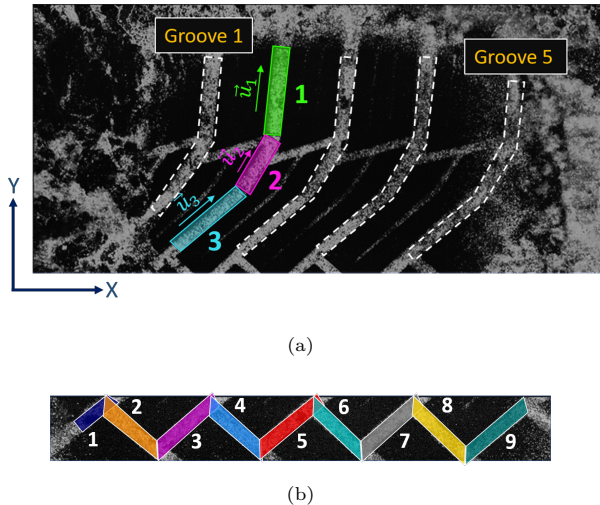


Fig. 13: Definition of the segments cutting and highlight of the new referential axis in each segment in Groove 2 (a) and segmentation of the zigzag central groove (b)

The evolution of $V_{u_{mean}}^* = V_{u_{mean}}/V_0$ with X/L_x inside the CPA is shown in Fig.14, for directional grooves (Figures 14(a), 14(b) and 14(c)), and for the central zigzag groove (Fig.14(d)). The results are remarkable, mainly for segment 1 of the directional grooves. Despite the small number of runs, the characteristic fluid velocity $V_{u_{mean}}^*$ of the fluid inside segment 1 is clearly correlated with X/L_x . The flow is pushed out of the groove at the beginning of the CPA, and sucked inside the segment at the end of the CPA; the maximum value of $V_{u_{mean}}^*$ is around 0.6. Such a correlation between fluid velocity inside a transverse groove and its location inside CPA has previously been established by Cabut et al. [15] considering the analysis of transverse type C-type grooves of a summer tire with four longitudinal grooves. In that case the correlation was nearly linear, there was no suction for grooves located at the end of the CPA, and the maximum normalized velocity was around 0.2, a value much smaller than the present one. The authors linked this behavior with the compression and relaxation of the rubber in the inlet and the outlet of the CPA, highlighting a parabolic distribution of the pressure at the shoulder [18]. A correlation between $V_{u_{mean}}^*$ and X/L_x is also clear for segments 1 and 2. For the central zigzag groove, the evolution of $V_{u_{mean}}^*$ with X/L_x shows a monotonic variation illustrating the accumulation of water from the front end of the CPA until its rear end.

18 3.2 Ensemble averaged velocity field

As a conclusion of this section, the discrepancies between winter-type and summer-type tires suggest that the different $V_{u_{mean}}^*$ profiles can be considered inside CPA as the hydrodynamic signature of the particular tread design considered.

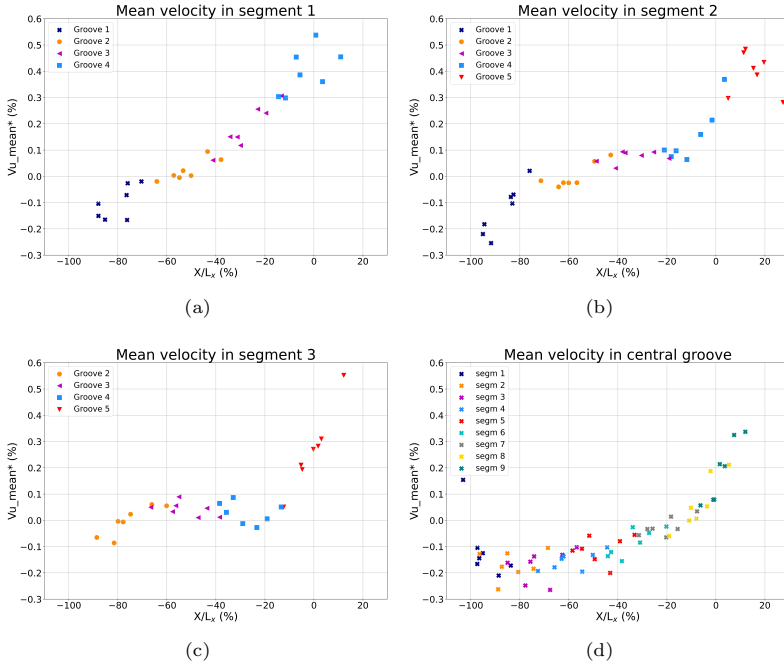


Fig. 14: Evolution of $V_{u_{mean}}^*$ over the grooves in the CPA in segment 1 (a), segment 2 (b), segment 3 (c) and zigzag groove (d) for $N=7$ runs, $V_0 = 11.11 m.s^{-1}$ and $H_w = 1.5 mm$

After studying the water flow inside the CPA, another region is of interest in this study, the water-bank. We draw the reader's attention to the random positioning of directional grooves inside the CPA. This adds an extra difficulty to consider averaged quantities inside this region. However, as stated in section 2.3, the overlapping of the N images has been done based on the position of the water-bank, thus our interest in averaged parameters in this last region of interest.

3.2 Ensemble averaged velocity field

In this section we analyze the velocity field of the ensemble averaged data for $N = 7$, $V_0 = 11.11 m.s^{-1}$ and $H_w = 1.5 mm$ to study the evolution of the velocity in the water-bank (WB). The areas of averaging are defined in such a way to detect the change in the global flow behavior as a function of

the position inside the WB. In particular, we want to check if there is some visible impact of the groove design on this part of the flow as a signature of the grooves.

3.2.1 Large scale movement inside the water-bank

The WB starts from $x = 0$ as indicated in Fig.5(b). To further analyze the evolution of V_x^* from the central region to the shoulders, we can plot it X-averaged in three zones splitting the WB between $x_1=0mm$ and $x_2=49mm$ as depicted in Fig.15(a). Such bands are chosen to cover the parts i) D_{x1} : from the WB beginning to before the peak of the longitudinal velocity shown in Fig.5(d), ii) D_{x2} around the peak value and iii) D_{x3} after such peak. The three regions are of equal width (Fig.15(a)). This allows us to study the evolution of the velocity profiles $V_x^*(y)$ and $V_y^*(y)$ at different x-positions as D_{x1} is the closest one and D_{x3} the furthest. We can hope to bring out some influence of the tread design on such profiles. The error bars represent the standard deviation over the N runs.

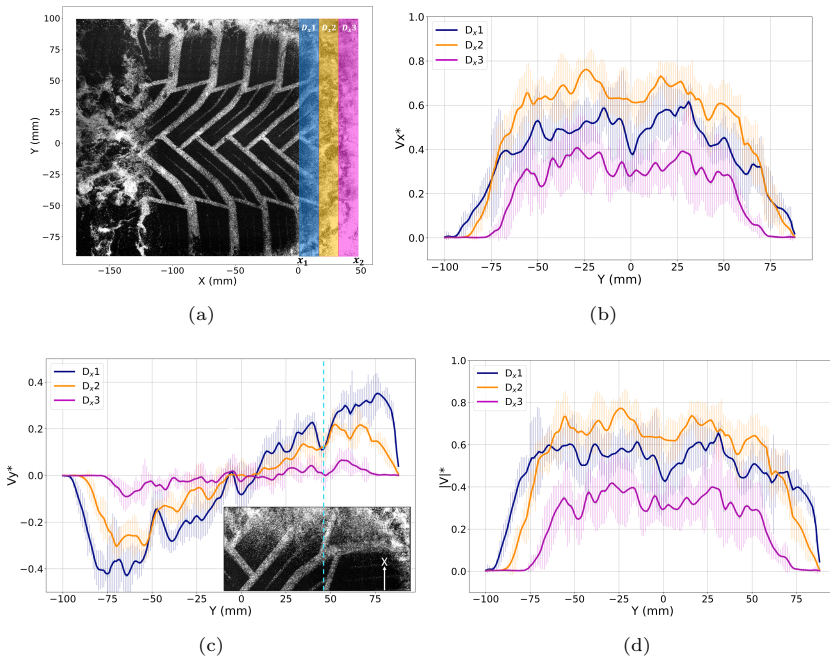


Fig. 15: The WB is divided here into three subregions of equal width D_{x1} , D_{x2} and D_{x3} highlighted in (a). The evolution of V_x^* (b), V_y^* (c) and $|V|^*$ (d) the velocity space X-averaged between x_1 and x_2 (a) is represented.

First we note that the profiles are not perfectly symmetric against $y = 0$. This is partly due to the asymmetry of the tread design in the transverse

direction. It can also be explained by the lack of repetitions that increases the noise in our signals. Second, for the three subregions $D_x i$, two humps exist for V_x^* (Fig.15(b)), reached around $y = -25mm$ and $y = 25mm$. The maximum of V_x^* is reached in $D_x 2$ and it exceeds 0.7. Concerning V_y^* (Fig.15(c)), we can see that at a large scale (tire width scale), the evolution is rather linear in the three subregions $D_x i$ and the highest values are reached in $D_x 1$. This is mainly due to the shape of the grooves that drain water to the shoulders rather than to the center. However, we can assimilate the disruptions specially seen in $D_x 1$ to a smaller scale phenomena.

3.2.2 Local or small scale groove influence inside the water-bank

We can see in the profile of V_y^* in $D_x 1$ (Fig.15(c)) that three “peak/hole” (P/H) events exist at $y = -48mm$, $y = 0$ and $y = 48mm$ (dashed blue line in Fig.15(c) for this last location). These disruptions correspond to the influence of the zigzag and the two connecting grooves on the flow in the WB. We emphasize that the subregion $D_x 1$ is outside the CPA, the tire is not in contact with the ground anymore and the flow in this region is therefore not enforced to channel inside the grooves. Such P/H characterizes the efficiency of the tread design to draw the water by the central and connecting grooves. At the present vehicle velocity V_0 , the P/H is no more present on the furthest bands $D_x 2$ and $D_x 3$. Note that the influence of the groove inlets is also visible on the longitudinal velocity profile for $D_x 1$ (Fig.15(b)), where we can observe a large velocity deficit. This loss is also visible in $D_x 2$ for which a plateau is present around $y = 0$. With more runs, the two other deficits could probably be determined at least for the band $D_x 1$. Such deficits in the two velocity profiles could be studied more precisely in the future to characterize water drained under the WB compared to the one ejected at the shoulders. Their global velocity evolution as a function of the car velocity will probably help in the design of tread efficiency.

3.2.3 Velocity magnitude inside the water-bank

We give in Fig.15(d) the evolution of the velocity magnitude $|V|^*$ spatially averaged along X between x_1 and x_2 . Globally, it has a shape close to V_x^* only that between $y = -50mm$ to $y = 50mm$, $|V|^*$ is rather homogeneous, meaning that in the region in front of the tire the direction of the water ejection changes from the center to the shoulders, but not its modulus. The deficit holes are more visible than for longitudinal velocity profiles but are less significant than for transverse velocity profiles. Nevertheless it seems that they are still present in the second band $D_x 2$ in location continuity with those in the band $D_x 1$. More runs will probably increase the trends.

In conclusion to this part, the transverse velocity profiles are more sensible to the tread design at local scale but the modulus is probably more robust

for the detection of their impact. At large scale, two humps exist around the center zone for the longitudinal velocity profiles only (not for the transverse velocity profiles) and are significantly maintained in all subregions $D_x i$. The linearity of V_y^* is also clear and maintained in all the WB width. However, at a small scale the grooves impact only the velocity profiles in the first band $D_x 1$.

4 Conclusion

In this work, we present some elements of a local investigation of the velocities involved during the rolling of a tire over a water film. We had a principal objective to refine the work by Cabut in order to obtain 1) parameters able to improve our knowledge about transition to the hydroplaning situation, 2) parameters able to highlight universal behaviors allowing tire comparison whatever the tread design studied. The r-PIV measurement technique has proven its efficiency in front of a rather complex tread design with inclined directional grooves and a central zigzag groove. The collapse over several independent runs of the velocity fields inside the water-bank is performed with a cross-correlation technique and allows to define a common coordinate system in which the position of the contact patch area is fixed, while the locations of the different grooves inside the contact patch area undergo from one run to the other a random spatial jitter parallel to the car motion. A segmentation of the directional and central zigzag grooves into elementary straight segments is performed and allows to deduce, for each element, from PIV measurements and for every run, a dimensionless characteristic velocity $V_{u_{mean}}^*$.

Results highlight a clear correlation between $V_{u_{mean}}^*$ inside an elementary segment and its dimensionless coordinate X/L_x where L_x is the contact patch length for the selected couple of operating parameters (V_0, H_w). This correlation is remarkably clear for the segments of the grooves close to the shoulders, with an ejection of water outside the grooves ($V_{u_{mean}}^* > 0$) for segments near the leading part of CPA, and a suction phenomenon ($V_{u_{mean}}^* < 0$) towards the grooves for segments located at the end of the CPA. However, the present results show some discrepancies with the case of a summer tire in a worn state with four longitudinal grooves and perpendicular transverse grooves for the sign and maximum value of $V_{u_{mean}}^*$ [15]. Finally, the velocity inside the water-bank has been studied using a statistical averaging over numerous trials, leading to specific hydrodynamic signature, at large and small scales, of the studied tread design. In the present work, for analyzing flow drainage from the center CPA zone to the CPA borders, we have shown extending Cabut's work that velocity averaged parameters (3.1.4 and 3.1.2) have to combine simultaneously both directional averaging in a flow zone of interest and longitudinal localization inside a transverse groove.

In the future, a parametric study should be carried out increasing car speeds until the appearance of hydroplaning. The interest of such a parametric study is twice. First, inside the CPA, it is of interest to study the evolution of $V_{u_{mean}}^*$ along the position X/L_x and see if there is a breaking point when reaching the

hydroplaning situation. Second, in the water-bank, the identification of suitable parameters e.g., the width of the WB allows us to study the efficiency of the tread until reaching its full capacity of drainage. The influence of H_w has also to be understood. Moreover, other tread designs should be included in further studies in order to examine designs' efficiency on a very local level. Last but not least, in parallel to the experimental approach, a numerical investigation is conducted in order to perform comparisons with experimental data concerning the different zones of interest [19].

Acknowledgments. This work is partly funded by the French government through the Association Nationale de la Recherche et de la Technologie (CIFRE grant agreement 2019/0949).

References

- [1] Horne, W.B., Dreher, R.C.: Phenomena of Pneumatic Tire Hydroplaning vol. 2056, (1963)
- [2] Maycock, G.: Second paper: Studies on the skidding resistance of passenger-car tyres on wet surfaces. Proceedings of the Institution of Mechanical Engineers: Automobile Division **180**(1), 122–157 (1965)
- [3] Meades, J.: Braking force coefficients obtained with a sample of currently available radial ply and crossed ply car tyres. Transportation research board (73) (1967)
- [4] Jenq, S.-T., Chiu, Y.-S., *et al.*: Transient hydroplaning performance of inflated radial tire with V-shape grooved tread pattern using ls-dyna explicit interactive fsi scheme. Journal of the Chinese Society of Mechanical Engineers **36**(2), 135–144 (2015)
- [5] Okano, T., Koishi, M.: Hydroplaning simulation using MSC. dytran. In: Proceedings of the 3rd European LS-DYNA Users Conference (2001)
- [6] Hermange, C., Oger, G., Le Chenadec, Y., Le Touzé, D.: A 3D SPH-FE coupling for FSI problems and its application to tire hydroplaning simulations on rough ground. Computer Methods in Applied Mechanics and Engineering **355**, 558–590 (2019)
- [7] Gillard, J.: An efficient partitioned coupling scheme for tire hydroplaning analysis. PhD thesis, Technische Universität München (2019)
- [8] Ong, G.P., Fwa, T.: Wet-pavement hydroplaning risk and skid resistance: modeling. Journal of Transportation Engineering **133**(10), 590–598 (2007)
- [9] Donatellis, M., Gelosa, E., Sangalli, R., Spinelli, M., Vitali, R.: Virtual

treaded tire simulation as a design predictive tool: Application to tire hydroplaning. In: 2009 SIMULIA Customer Conference (2009)

- [10] Allbert, B.: Tires and hydroplaning. SAE Transactions, 593–603 (1968)
- [11] Hermange, C., Todoroff, V., Biesse, F., Le-Chenadec, Y.: Experimental investigation of the leading parameters influencing the hydroplaning phenomenon. *Vehicle System Dynamics*, 1–18 (2021)
- [12] Cabut, D., Michard, M., Simoëns, S., Todoroff, V., Hermange, C., Le-Chenadec, Y.: PIV measurements using refraction at a solid–fluid interface. *Measurement Science and Technology* **32**(3), 035205 (2020)
- [13] Cabut, D.: Characterisation of the flow in a water-puddle under a rolling tire with refracted piv method. PhD thesis, Lyon (2020)
- [14] Cabut, D., Michard, M., Simoëns, S., Todoroff, V., Lemaître, J., Hermange, C., Le Chenadec, Y.: Particle image velocimetry (PIV) measurements in a water film, application to a tire rolling through a puddle. *Mechanics & Industry* **20**(8), 811 (2019)
- [15] Cabut, D., Michard, M., Simoëns, S., Mees, L., Todoroff, V., Hermange, C., Le Chenadec, Y.: Analysis of the water flow inside tire grooves of a rolling car using refraction particle image velocimetry. *Physics of Fluids* **33**(3), 032101 (2021)
- [16] Croner, E.: Etude de l'écoulement autour des ensembles roulants d'un véhicule en vue de l'optimisation aérodynamique du pneumatique. PhD thesis, Toulouse, ISAE (2014)
- [17] Reiß, J., Sebald, J., Haag, L., Zander, V., Indinger, T.: Experimental and numerical investigations on isolated, treaded and rotating car wheels. Technical report, SAE Technical Paper (2020)
- [18] Heinrich, G., Klüppel, M.: Rubber friction, tread deformation and tire traction. *Wear* **265**(7-8), 1052–1060 (2008)
- [19] Ben Khodja, A., Oger, G., Hermange, C., Simoëns, S., Poncet, C., Michard, M., Le Touzé, D.: Validation of coupled SPH-FE hydroplaning simulations using PIV measurements, In Proceedings of the 15th international SPHERIC workshop, pp. 417–424 (June 2021)